IMAGE-BASED MODELING OF THE SKIN-FRICTION COEFFICIENT IN COMPRESSIBLE BOUNDARY-LAYER TRANSITION

Wenjie Zheng
State Key Laboratory of Turbulence and Complex Systems
College of Engineering, Peking University
Beijing 100871,China
jswj@pku.edu.cn

Yue Yang
State Key Laboratory of Turbulence and Complex Systems
College of Engineering, Peking University
Beijing 100871,China
yyg@pku.edu.cn

Shiyi Chen
State Key Laboratory of Turbulence and Complex Systems
College of Engineering, Peking University
Beijing 100871,China
syc@pku.edu.cn

ABSTRACT

We report a geometric study of Lagrangian structures in compressible, spatially evolving transitional boundary layers at two Mach numbers $Ma_\infty = 2.25$ and 6, and develop a simple model of the skin-friction coefficient based the geometric analysis of two-dimensional scalar images. The velocity fields are obtained by the direct numerical simulation (DNS). The Lagrangian structures in the transition process are extracted from the Lagrangian scalar field by a sliding window filter in compact frames. The multi-scale and multi-directional geometric analysis is applied to characterize the averaged inclination angles of Lagrangian structures at different scales ranging from the boundary layer thickness to several viscous length scales, where the inclination angle is on the plane of the streamwise and wall-normal directions. In general, the averaged inclination angle is increased along the streamwise direction, and the variation of the angles for large-scale structures is smaller than that for small-scale structures. We develop a simple model of skin-friction coefficient based on the inclination angle statistics of the filtered component fields on the streamwise and wall-normal plane at different scales. The trend of the increasing averaged inclination angle is qualitatively similar to the rise of the skin-friction coefficient, and our modelled skin-friction coefficient agrees well quantitatively with the DNS results for the two Mach numbers.

INTRODUCTION

The prediction on the skin-friction coefficient c_f in compressible boundary layers is critically important for the design of high-speed vehicles and propulsion systems. The boundary-layer transition has a strong influence on aerodynamic drag and heating, because much higher friction and heating can be generated on the surface of aerospace vehicles in turbulent flows than those in laminar flows. Despite considerable efforts in theoretical, experimental, and numerical studies, the reliable prediction of the skin-friction coefficient in compressible boundary layers is still challenging (Zhong & Wang, 2012).

Theoretical study on the empirical formula of c_f in compressible boundary layers is restricted in laminar or fully turbulent states. For compressible laminar boundary layers, the empirical formula of c_f is well established (van Driest, 1952). For compressible turbulent boundary layers, the empirical formula of c_f is transformed from that in incompressible turbulent boundary layers (van Driest, 1956; Spalding & Chi, 1964; White & Christoph, 1972).

On the other hand, there is lack of theoretical models for the laminar-to-turbulent transition stage. The existing approximate models for predicting transition, such as the e^N-method and parabolized stability equations (Herbert, 1997), are relied on empirical input or specific initial conditions. In addition, c_f is not easy to be measured experimentally in compressible boundary layers (Goyne et al., 2003). Despite the considerable effort devoted to skin-friction measurement and the wide variety of available techniques, all seem to suffer problems related to accuracy, repeatability and practicality (Hutchins & Choi, 2002).

For the numerical simulations of compressible transitional boundary layers, direct numerical simulation (DNS) is useful for understanding transition mechanisms and evaluating transition-prediction methods (Zhong & Wang, 2012), but the DNS is computationally expensive. Large-

1

eddy simulation (LES) reduces the computational cost by filtering small-scale motions, but its accuracy for the transition is influenced by the resolution of grids or the wall models (Ducros *et al.*, 1996). The method of Reynolds-averaged Navier–Stokes (RANS) equations with low computational cost usually requires *a priori* information of the transition point, so it is not a complete predictive tool (Wang & Fu, 2009).

In the present study, we develop a simple model of the skin-friction coefficient c_f based the multi-scale and multi-directional analysis of two-dimensional scalar images which is relatively easy to be obtained in experiments by imaging techniques. The Lagrangian scalar field is used as an ideal tracer scalar without diffusion, which can reveal rich geometry of scalar structures. This method have been applied in isotropic turbulence (Yang *et al.*, 2010), Taylor-Green and Kida-Pelz flows (Yang & Pullin, 2010), the K-type transition in channel flow (Zhao *et al.*, 2016), fully developed channel flows (Yang & Pullin, 2011), and the transition in a weakly compressible boundary layer (Zheng *et al.*, 2016). With the tracking of the Lagrangian scalar field, a geometric diagnostic methodology (Yang & Pullin, 2011) based on the mirror-extended curvelet transform (Candes *et al.*, 2006) is applied to characterize the evolutionary geometry of Lagrangian structures within the sliding window (Zheng *et al.*, 2016). Finally we develop a predictive model of c_f based on the quantified multi-scale scalar geometry.

SIMULATION DETAILS
Direct Numerical Simulation

The DNS of the spatially evolving flat-plate boundary layers at two Mach numbers $Ma_\infty = 2.25$ and 6 is performed by solving the compressible Navier–Stokes (N–S) equations using the OpenCFD code (Li *et al.*, 2010). The convection terms in compressible N–S equations are approximated by a seventh-order WENO scheme, and the viscous terms are approximated by an eighth-order central finite difference scheme. The time evolution is advanced by the third-order TVD Runge–Kutta method.

As shown in figure 1, the computational domain is bounded by an inlet boundary and a non-reflecting outlet boundary in the streamwise *x*-direction, a wall boundary and a non-reflecting upper boundary in the wall-normal *y*-direction, and two periodic boundaries in the spanwise *z*-direction. The inlet boundary is given by a laminar compressible boundary-layer similarity solution. In order to trigger the laminar-to-turbulent transition, an upstream region of blowing and suction is introduced near the inlet. The non-slip isothermal boundary condition is used at the wall.

The parameters of the DNS are listed in Table 1. The subscript "∞" denotes the free stream properties, and "w" denotes the quantities on the wall. The free stream Mach number is $Ma_\infty \equiv U_\infty/c_\infty$, where c_∞ is the free stream sound speed. The free stream Reynolds number is $Re_\infty \equiv \rho_\infty U_\infty L/\mu_\infty$, where $L = 1$ inch is the reference length. The sizes of the computation domain are $L_x \times L_y \times L_z$, which are nondimensionalized by L. The domain is discretized using grids $N_x \times N_y \times N_z$ with grid spacings $\Delta x \times \Delta y \times \Delta z$. The superscript "$+$" denotes the quantities normalized by the viscous length scale $\delta_v \equiv \mu_w/(\rho_w u_\tau)$ with the friction velocity u_τ at the fully developed turbulent state.

The present DNS results are validated with existing ex-
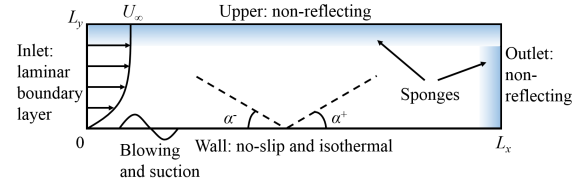
Figure 1: A schematic diagram of the computational domain with boundary conditions and the inclination angles of structures. Possible inclined structures are sketched by dashed lines.

perimental and numerical results. The mean flow statistics in the fully-developed turbulent region from DNS are shown in figure 2, and they agree well with the experimental (not shown) and DNS results in Pirozzoli *et al.* (2004). Here, the overbar denotes the Reynolds average over the spanwise direction. Figure 3 shows the skin-friction coefficient $c_f \equiv \tau_w/(\frac{1}{2}\rho_\infty U_\infty^2)$ along the streamwise direction. The rapid increase of c_f signals the transition, and this appears to be related to the generation of three-dimensional vortices and the breakdown of large-scale coherent structures. The regions between laminar and turbulent regimes are roughly at $x = 2 \sim 4$ and $x = 3 \sim 5$ for $Ma_\infty = 2.25$ and $Ma_\infty = 6$, respectively. Figure 4 shows the normalized mean velocity profiles and their van Driest transforms at $x = 7$ with theoretical fits. The van Driest transformed mean velocity is $\bar{u}_{vd} = \int_0^{\bar{u}}(\bar{\rho}/\bar{\rho}_w)^{1/2}\mathrm{d}\bar{u}$. The tails of two-point correlations of the velocity components in the spanwise direction are sufficiently small at lateral boundaries (not shown), which ensures that L_z is large enough so that the imposed periodic boundary condition does not affect flow statistics (Pirozzoli *et al.*, 2004).

Lagrangian Scalar Field

The three-dimensional Lagrangian scalar field $\phi(\boldsymbol{x},t)$ is a passive tracer field, and iso-surfaces of ϕ are material surfaces in the temporal evolution. We remark that ϕ is a passive scalar field that is similar to temperature or species concentration, but it has no diffusivity so that it can display rich geometry of flow structures at very fine scales. The scalar field is governed by the pure convection equation

$$\frac{\partial \phi}{\partial t} + \boldsymbol{u}\cdot\nabla\phi = 0, \tag{1}$$

which is solved by the backward-particle-tracking method (Yang *et al.*, 2010; Yang & Pullin, 2011).

In the backward-particle-tracking method, the trajectories of fluid particles are calculated by solving the kinematic equation

$$\frac{\partial \boldsymbol{X}(\boldsymbol{x}_0,t_0|t)}{\partial t} = \boldsymbol{V}(\boldsymbol{x}_0,t_0|t) = \boldsymbol{u}(\boldsymbol{X}(\boldsymbol{x}_0,t_0|t),t), \tag{2}$$

where $\boldsymbol{X}(\boldsymbol{x}_0,t_0|t)$ is the location at time t of a fluid particle which was located at $\boldsymbol{x}_0$ at the initial time t_0, $\boldsymbol{V}(\boldsymbol{x}_0,t_0|t)$ is the Lagrangian velocity of the fluid particle, and $\boldsymbol{u}(\boldsymbol{X}(\boldsymbol{x}_0,t_0|t),t)$ is its local Eulerian velocity.

The backward-particle-tracking method (see Yang *et al.*, 2010) is numerically stable and has no numerical dissipation, which can ensure the mass conservation within a

Table 1: DNS parameters.

Ma_∞	Re_∞	T_w/T_∞	T_∞ (K)	$L_x \times L_y \times L_z$	$N_x \times N_y \times N_z$	$\Delta x^+ \times \Delta y_w^+ \times \Delta z^+$
2.25	6.35×10^5	1.90	169.44	$12 \times 0.6 \times 0.2$	$4800 \times 200 \times 320$	$11.30 \times 0.91 \times 5.65$
6	1.69×10^6	6.98	169.44	$12 \times 0.6 \times 0.2$	$4800 \times 200 \times 320$	$4.62 \times 0.37 \times 2.31$
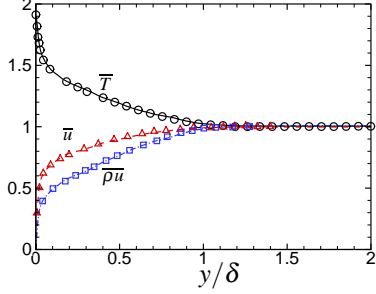
Figure 2: Mean profiles in the fully-developed turbulent region at $Ma_\infty =$ 2.25 (lines: present DNS; symbols: DNS in Pirozzoli *et al.* (2004)).
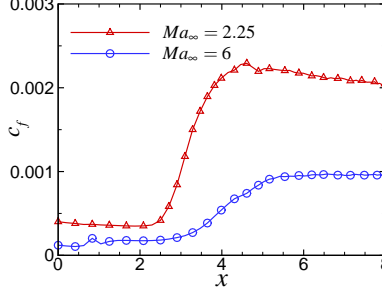
Figure 3: Skin-friction coefficient.
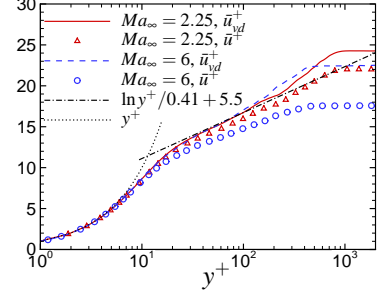
Figure 4: Mean velocity profile normalized by the wall shear velocity at $x = 7$.

closed material surface. In the numerical implementation, this method is used to calculate the Lagrangian scalar field at a given time t as follows (Zheng *et al.*, 2016).

(1) The full Eulerian velocity field on the grids $N_x \times N_y \times N_z$ within a time interval from t_0 to $t > t_0$ is solved and then stored in disk. The time step is selected by $\Delta t \leqslant \delta_\nu/u_\tau$ to capture the finest resolved scales in the velocity field.

(2) At the given time t, particles are placed at the uniform grid points of $N_x^p \times N_y^p \times N_z^p$ in the subdomain of interest for further geometric analysis. In principle, the time interval $\Delta T \equiv t - t_0$ for backward particle-tracking should be selected to ensure that all the particles at the outlet boundary of the subdomain can travel backward to the inlet location $x = 0$, but in the spatially developed wall flows, it can take very long time for the particles very close to the wall traveling back to x_0 owing to the very small streamwise velocity. In the implementation, we find that the statistical results are not sensitive to the value of ΔT for $\Delta T \geqslant 1$ from numerical experiments. Therefore, we set $\Delta T = 1$ to greatly reduce the computational cost with negligible deviations.

(3) The particles are released and their trajectories are calculated backward in time within ΔT or until they arrive at $x_0 = 0.2$, where the initial material surfaces are considered as flat sheets. A three-dimensional, fourth-order Lagrangian interpolation scheme is used to obtain fluid velocity at the location of each particle, and an explicit, second-order Adams-Bashforth scheme is applied for the time integration.

(4) After the backward tracking, we can obtain initial locations x_0 of the particles and the flow map

$$F_t^{t_0}(\boldsymbol{X}) : \boldsymbol{X}(x_0, t_0|t) \mapsto \boldsymbol{x}_0, \quad t \geqslant t_0. \qquad (3)$$

Then the Lagrangian field $\phi(\boldsymbol{x}, t)$ at any given time t can be obtained as

$$\phi(\boldsymbol{x}, t) = \phi(F_t^{t_0}(\boldsymbol{X}), t_0) = \phi(\boldsymbol{x}_0, t_0). \qquad (4)$$

The initial Lagrangian field is uniquely determined as

$\phi(\boldsymbol{x}_0, t_0) = y$ based on the criteria (Zhao *et al.*, 2016) of the best approximation to vortex sheets and geometric invariance of ϕ in the laminar state.

Diagnostic Methodologies

For the diagnostic of flow structures, a sliding window filter developed in Zheng *et al.* (2016) is used to extract the spatially evolving Lagrangian structures and capture their major deformations in compact frames at different streamwise locations. The filter is defined as

$$f(x) = \exp\left[-n\left(\frac{x - x_c}{l_w}\right)^n\right], \qquad (5)$$

where x_c is the central position of the window, l_w is the width of the window, and n is a positive even integer. Figure 5 illustrates typical profile of the proposed filter. From Eq. (5), the window width $l \equiv 2(x - x_c)$ of the filter at the value f is

$$\frac{l}{l_w} = 2\exp\left[\frac{\ln(-\ln f/n)}{n}\right]. \qquad (6)$$

The two-dimensional scalar field for further analysis is extracted within a compact region with the cutoff window width $l = l_c$ and $f = 0.0001$ at the boundaries. Moreover, the major features of the extracted scalar field with large scalar gradient $\nabla\phi$ are captured within the subdomain with the effective window width $l = l_e$ and $f \geqslant 0.9$. As shown in figure 5, we choose $n = 16$ to smooth the transition of f from $f = 0$ to 1 with $l_c/l_w = 1.93$ and $l_e/l_w = 1.46$, and we fix the effective window width as $l_e = 1$.

With given x_c and l_w, the extracted Lagrangian scalar field $\phi_f(\boldsymbol{x}, t)$ can be obtained as

$$\phi_f(\boldsymbol{x}, t) = \phi(\boldsymbol{x}, t)f + \phi(\boldsymbol{x}_0, t_0)(1 - f). \qquad (7)$$

3
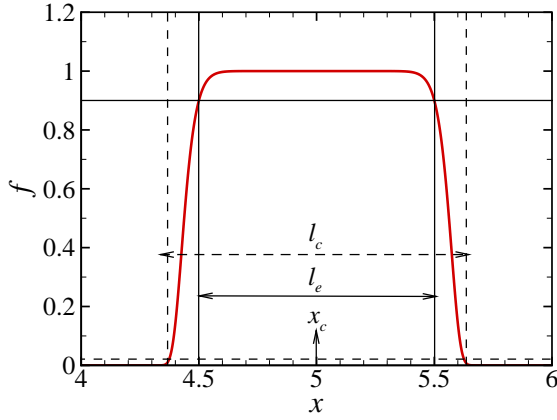
Figure 5: Profile of the sliding window function to extract ϕ_f from the entire ϕ.

(a) $Ma_\infty = 2.25$

(b) $Ma_\infty = 6$

Figure 6: Instantaneous Lagrangian fields on the x–y plane in the transitional boundary layers at two Mach numbers.

The extracted Lagrangian field in the sliding window has a smooth transition from an evolving scalar $\phi(\boldsymbol{x},t)$ to the initial scalar $\phi(\boldsymbol{x}_0,t_0)$ at window boundaries. Thus, the boundary condition of the window in the streamwise direction can be considered as periodic for the fast Fourier transform (FFT).

The multi-scale and multi-directional geometric analysis (Yang & Pullin, 2011) is applied to characterize the evolutionary geometry of ϕ within the sliding window and on a series of streamwise and wall-normal (x–y) planes. This provides quantitative statistics on the inclination angle of Lagrangian structures at different scales and streamwise locations during the transition.

Geometric features of a two-dimensional scalar field can be extracted at a characteristic length scale $\mathscr{L}_j = 2^{-j}, j \in \mathbb{N}$ and the averaged deviation angles away from the horizontal axis at each scale j in physical space. As shown in figure 1, we define the inclination angle α between an inclined structure projected on the streamwise and wall-normal (x–y) plane and the x-direction. The normalized characteristic length scales of structures in the multi-scale decomposition are given in Table 2. Subsequently, $\mathscr{L}_j \geqslant 0.5\delta$ will be referred to as "large scale", $\mathscr{L}_j \leqslant 100\delta_v$ as "small scale", and in between as "intermediate scale".

RESULTS
Lagrangian Structures on the Streamwise and Wall-normal Plane

Instantaneous Lagrangian fields on the x–y plane in the transition process at two Mach numbers are shown in figure 6. The vortical structures are generated at the wall and then lifted to form inclined structures.

Figure 7 illustrates the multi-scale decomposition of a Lagrangian field on the x–y plane. The original field is extracted by the sliding window filter within the transitional region at $x = 3 \sim 4$ for $Ma_\infty = 6$. The characteristic length scale $\mathscr{L}_j$ for each scale index j is quantified in Table 2. The averaged inclination angle $\langle\alpha\rangle$ is calculated from 10 x–y planes at equispaced spanwise locations using the multi-directional decomposition with curvelet window functions (Yang & Pullin, 2011), and the results are sketched by dashed lines in figure 7. We find that the filtered component fields at different scales show different preferential orientations as the observation in Zheng *et al.* (2016). In general,
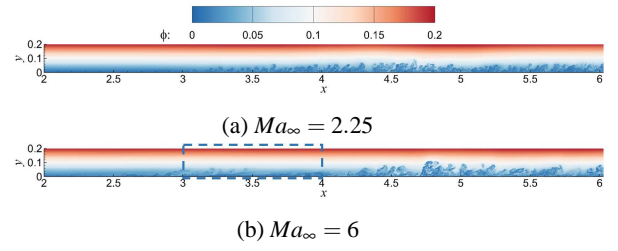
the averaged inclination angle $\langle\alpha\rangle$ increases with the decreasing length scales.

(a) Original

(b) Scale 6

(c) Scale 7

(d) Scale 8
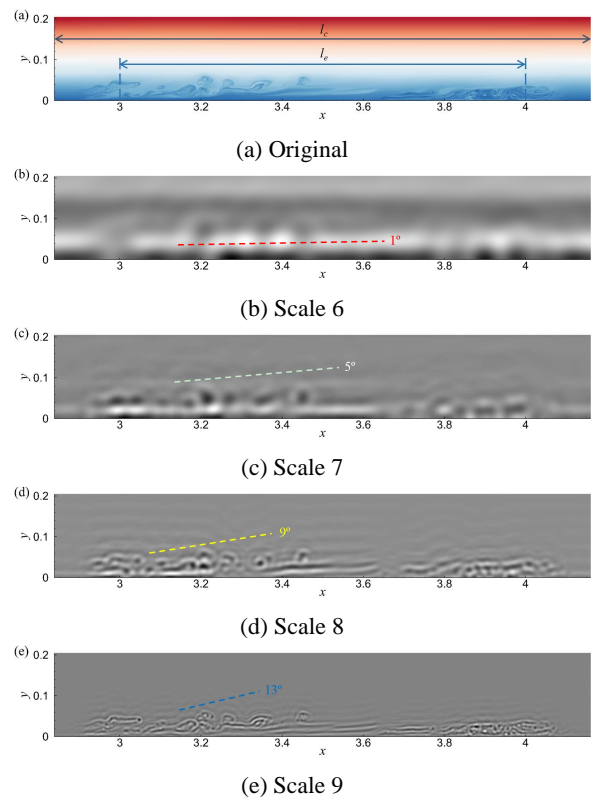
(e) Scale 9

Figure 7: Scale decomposition of the Lagrangian field on the x–y plane in a transitional boundary layer at $Ma_\infty = 6$. The cutoff and effective window widths l_c and l_e for the sliding window filter are marked. Averaged inclination angles calculated from multi-scale geometric analysis are sketched in dashed lines.

Image-based Modeling of the Skin-friction Coefficient

From the inclination-angle statistics of the filtered component fields on the x–y plane at different scales, we propose a simple image-based model of the skin-friction co-

4

Table 2: Characteristic length scales $\mathscr{L}_j = 2^{-j}$ with the scale index j are normalized by the boundary-layer thickness δ and viscous length scale δ_v.

Ma_∞	Length	Scale 1	Scale 2	Scale 3	Scale 4	Scale 5	Scale 6	Scale 7	Scale 8	Scale 9
2.25	$\mathscr{L}_j/\delta$	5.56	2.78	1.39	0.694	0.347	0.174	0.0868	0.0434	0.0217
	$\mathscr{L}_j/\delta_v$	4545	2273	1136	568	284	142	71.0	35.5	17.8
6	$\mathscr{L}_j/\delta$	5	2.5	1.25	0.625	0.313	0.156	0.0781	0.0391	0.0195
	$\mathscr{L}_j/\delta_v$	1825	912	456	228	114	57.0	28.5	14.3	7.13

efficient as

$$c_f(x,\mathscr{L}_j) = \frac{c_{f,T}(\overline{x_T}) - c_{f,L}(\overline{x_L})}{\langle\alpha(\overline{x_T},\mathscr{L}_j)\rangle}\langle\alpha(x,\mathscr{L}_j)\rangle + c_{f,L}(\overline{x_L}),$$
(8)

where the subscript "L" denotes laminar quantities, and "T" denotes quantities in the fully-developed turbulent region. In particular, reference locations $\overline{x_L}$ and $\overline{x_T}$ of laminar and fully turbulent states are determined from the profiles of $\langle\alpha(x,\mathscr{L}_j)\rangle$. The averaged inclination angle is almost $0°$ at $\overline{x_L}$ in the laminar state, and increases sharply in the transitional region. Finally it converges to a statistically steady value at $\overline{x_T}$ in the fully turbulent state.

The value of modelled c_f is bounded by the empirical formulae at two extreme states. The compressible laminar skin friction $c_{f,L}$ is evaluated as

$$c_{f,L}(x) = \frac{0.664}{\sqrt{Re_x^*}}$$
(9)

with $Re_x^* = \rho^* U_\infty x/\mu^*$ (see Anderson, 2010) at the reference temperature T^*

$$T^* = 1 + 0.032 Ma_\infty^2 + 0.58(T_w - 1).$$
(10)

The formula for turbulent skin-friction used here is

$$c_{f,T}(x) = \frac{0.455}{S^2}\left[\ln\left(\frac{0.06}{S}Re_x\frac{1}{\mu_w}\sqrt{\frac{1}{T_w}}\right)\right]^{-2}$$
(11)

with $Re_x \equiv Re_\infty x$, $S = \frac{\sqrt{T_w-1}}{\sin^{-1}A}$ and $A = \left(r\frac{\gamma-1}{2}Ma_\infty^2\frac{1}{T_w}\right)^{1/2}$ (see White, 2006).

As shown in figure 8, we use the absolute error

$$\varepsilon_a = \frac{\int_l |c_{f,model} - c_{f,DNS}|\, dx}{l}$$
(12)

and the relative error

$$\varepsilon_r = \frac{\int_l |c_{f,model} - c_{f,DNS}|\, dx/l}{\int_l c_{f,DNS}\, dx/l} \times 100\%$$
(13)

to evaluate the image-based model Eq. (8) based on averaged inclination angles at different length scales. The minimum error of the model is achieved at the length scale $\mathscr{L}_j$ between $10\delta_v$ and $50\delta_v$ for two Mach numbers.

Based on the error analysis, we use the values of $\langle\alpha\rangle$ at the length scale $\mathscr{L}_j \approx 30\delta_v$ in the model Eq. (8). The physical assumption for this model is that the lift of vortical structures during the transition, usually as the generation of inclined, tube-like structures, can generate inclined strong shear layers (Zhao *et al.*, 2016) and induce the negative streamwise velocity to increase c_f. As shown in figure 9, the trend of the increasing averaged inclination angle is qualitatively similar to the rise of c_f, and the modelled c_f in Eq. (8) agrees well quantitatively with DNS results for both Mach numbers. This implies that it is possible to quantify c_f, which is hard to be measured in high-Ma boundary-layer transition, from two-dimensional scalar images that are relatively easy to be obtained from experiments.

CONCLUSIONS

A simple model of the skin-friction coefficient is proposed based on the inclination angle statistics of the Lagrangian fields on the streamwise and wall-normal plane at different scales. The DNS of the spatially evolving flat-plate boundary layers is performed at two Mach numbers $Ma_\infty = 2.25$ and 6. The Lagrangian scalar field is the calculated in the high speed transitional boundary layers. The multi-scale and multi-directional geometric analysis with the sliding window filter are applied to characterize the geometry of spatially evolving Lagrangian structures. The averaged inclination angle is increased along the streamwise direction, and the trend is qualitatively similar to the rise of the skin-friction coefficient. The modelled skin-friction coefficient agrees well quantitatively with DNS results for both Mach numbers. The minimum error of the model is achieved at the length scale $\mathscr{L}_j$ between $10\delta_v$ and $50\delta_v$. The applicability of our proposed image-based model will be investigated extensively with experimental imaging in the future work.

REFERENCES

Anderson, J. D. 2010 *Fundamentals of aerodynamics*, 4th edn. New York: McGraw-Hill.

Candes, E., Demanet, L., Donoho, D. & Ying, L. 2006 Fast discrete curvelet transforms. *Multiscale Model. Simul.* **5**, 861–899.

van Driest, E. R. 1952 Investigation of laminar boundary layer in compressible fluids using the Crocco method. *Tech. Rep.* 2597. NACA Tech. Note.

van Driest, E. R. 1956 The problem of aerodynamic heating. *Aeronaut. Engng Rev.* **15**, 26–41.

Ducros, F., Comte, P. & Lesieur, M. 1996 Large-eddy simulation of transition to turbulence in a boundary layer de-
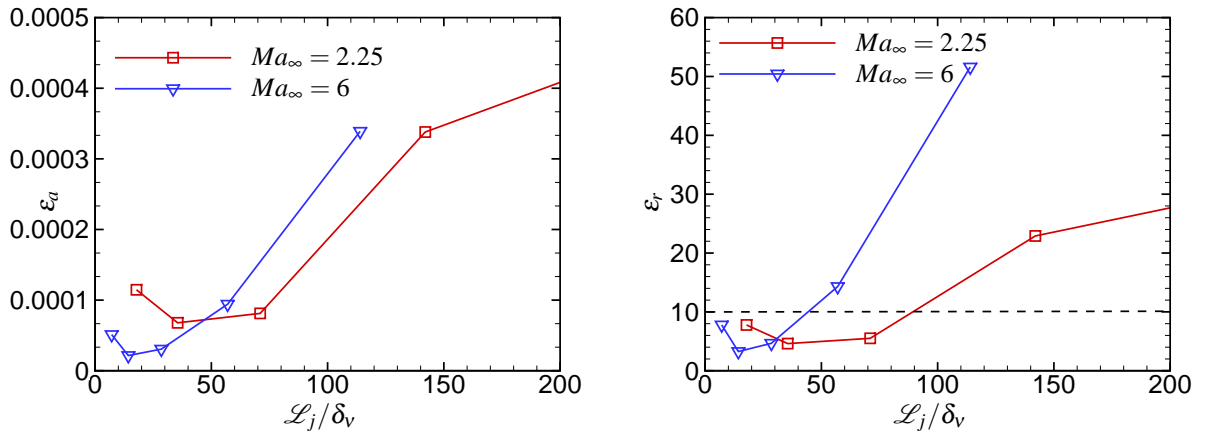
Figure 8: Error of the skin-friction coefficients from the image-based model in Eq. (8) at different length scales.

(a) $Ma_\infty = 2.25$

(b) $Ma_\infty = 6$
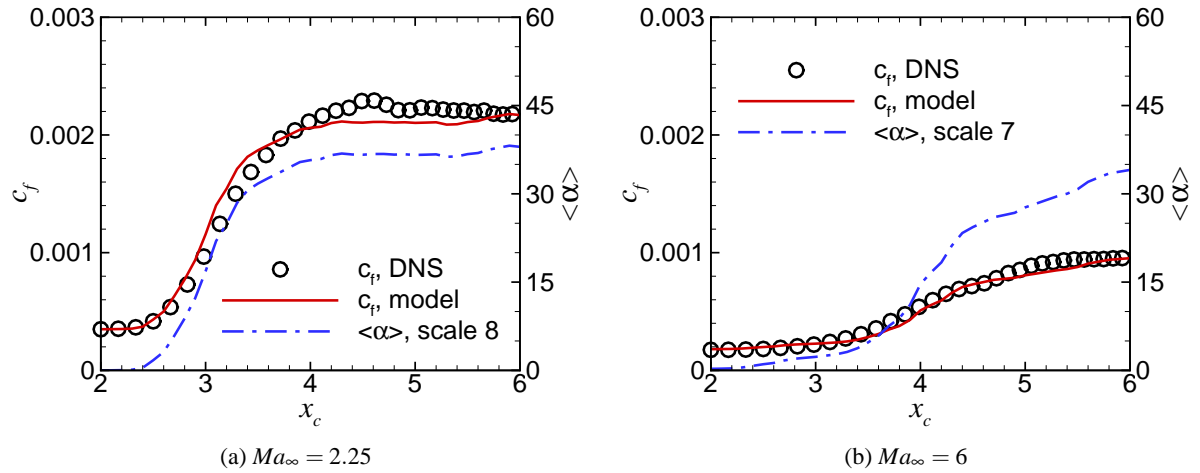
Figure 9: Comparison of the skin-friction coefficients from DNS and the image-based model in Eq. (8) at different Ma_∞, along with the averaged inclination angle of Lagrangian structures with the characteristic length scale $\mathscr{L}_j \approx 30\delta_v$.

veloping spatially over a flat plate. *J. Fluid Mech.* **326**, 1–36.

Goyne, C. P., Stalker, R. J. & Paull, A. 2003 Skin-friction measurements in high-enthalpy hypersonic boundary layers. *J. Fluid Mech.* **485**, 1–32.

Herbert, T. 1997 Parabolized stability equations. *Annu. Rev. Fluid Mech.* **29**, 245–283.

Hutchins, N. & Choi, K.-S. 2002 Accurate measurements of local skin friction coefficient using hot-wire anemometry. *Prog. Aerosp. Sci.* **38**, 421–446.

Li, X., Fu, D. & Ma, Y. 2010 Direct numerical simulation of hypersonic boundary layer transition over a blunt cone with a small angle of attack. *Phys. Fluids* **22**, 025105.

Pirozzoli, S., Grasso, F. & Gatski, T. B. 2004 Direct numerical simulation and analysis of a spatially evolving supersonic turbulent boundary layer at $M = 2.25$. *Phys. Fluids* **16**, 530.

Spalding, D. B. & Chi, S. W. 1964 The drag of a compressible turbulent boundary layer on a smooth flat plate with and without heat transfer. *J. Fluid Mech.* **18**, 117–143.

Wang, L. & Fu, S. 2009 Modelling flow transition in a hypersonic boundary layer with Reynolds-averaged Navier-Stokes approach. *Sci. China Ser. G-Phys. Mech. Astron.* **52**, 768–774.

White, F. M. 2006 *Viscous Fluid Flow*, 3rd edn. New York: McGraw-Hill.

White, F. M. & Christoph, G. H. 1972 A simple theory for the two-dimensional compressible turbulent boundary layer. *J. Basic Eng.* **94**, 636–642.

Yang, Y. & Pullin, D. I. 2010 On Lagrangian and vortex-surface fields for flows with Taylor–Green and Kida–Pelz initial conditions. *J. Fluid Mech.* **661**, 446–481.

Yang, Y. & Pullin, D. I. 2011 Geometric study of Lagrangian and Eulerian structures in turbulent channel flow. *J. Fluid Mech.* **674**, 67–92.

Yang, Y., Pullin, D. I. & Bermejo-Moreno, I. 2010 Multi-scale geometric analysis of Lagrangian structures in isotropic turbulence. *J. Fluid Mech.* **654**, 233–270.

Zhao, Y., Yang, Y. & Chen, S. 2016 Evolution of material surfaces in the temporal transition in channel flow. *J. Fluid Mech.* **793**, 840–876.

Zheng, W., Yang, Y. & Chen, S. 2016 Evolutionary geometry of Lagrangian structures in a transitional boundary layer. *Phys. Fluids* **28**, 035110.

Zhong, X. & Wang, X. 2012 Direct numerical simulation on the receptivity, instability, and transition of hypersonic boundary layers. *Annu. Rev. Fluid Mech.* **44**, 527–561.

6